SUPPORTING INFORMATION

Characterization and Visualization of Vesicles in the Endo-Lysosomal Pathway with Surface-Enhanced Raman Spectroscopy and Chemometrics

Anna Huefner[♪‡†], *Wei-Li Kuan*[†], *Karin H. Müller*[§], *Jeremy N. Skepper*[§], *Roger A. Barker*[†], *Sumeet Mahajan*[‡*]

[♪]Sector for Biological and Soft Systems, Cavendish Laboratory, Department of Physics, University of Cambridge, 19 JJ Thomson Avenue, Cambridge, CB3 0HE, United Kingdom

[‡]Institute of Life Sciences and Department of Chemistry, University of Southampton, Highfield Campus, SO17 1BJ, Southampton, United Kingdom

[†]John van Geest Centre for Brain Repair, University of Cambridge, Forvie Site, Robinson Way, Cambridge, CB2 0PY, United Kingdom

[§]Cambridge Advanced Imaging Centre, Dept. of Physiology, Development and Neuroscience, Anatomy Building, Cambridge University, Downing Street, Cambridge CB2 3DY, UK

Intracellular localization of AuNPs. Following AuNP incubation for 72 h, cells were fixed and images collected using TEM in order to localize intracellular AuNPs as seen in Figure S1. All intracellular particles were found in membrane-bound vesicles such as endosomes, phagosomes, phagolysosomes and lysosomes. Red arrows indicate examples of particles localized in the endosomes and phagosomes. In Figure S1A-B, vesicle enclosing particles (here a secondary lysosome and phagolysosome) can be seen near the nucleus (n) and the Golgi apparatus (g).

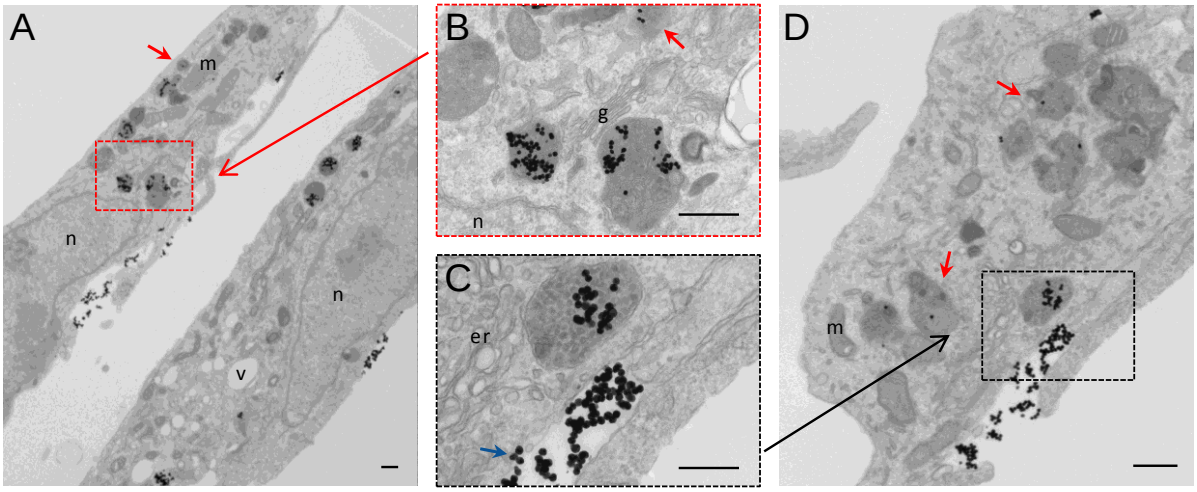

Figure S1: Localization of AuNPs inside cells after an incubation pulse of 72 h. Particles are found inside endosomes (marked with red arrows), phagosomes, phagolysosomes and lysosomes with a localization close to the nucleus (A) and the Golgi apparatus (B). Primarily, particle intake involves endocytosis and phagocytosis (C and D) as indicated by the blue arrow (C). All scale bars: 500 nm, abbr.: n: nucleus, m: mitochondria, v: vacuole, er: endoplasmic reticulum, g: Golgi apparatus.

TEM micrographs in Figure S1C-D suggest nanoparticle uptake *inter alia via* endocytosis and phagocytosis (blue arrow).

Cellular viability after AuNP incubation. Despite having internalized AuNPs, cells appeared healthy with an intact cell membrane and well-preserved cytoplasmic organelles (see main manuscript, Figure 2). Although no morphological features of apoptosis (e.g. highly condensed chromatin in the nucleus, formation of apoptotic bodies in the cytoplasm) or necrosis (e.g. swollen mitochondria, loss of plasma membrane integrity)[1, 2] were observed, the vital state of the cells was formally assessed. Therefore, the results from two separate cell viability assays were considered to evaluate the integrity of the plasma membrane and the metabolic state of the cell, respectively, as shown in Figure S2. We compared cell samples which had not been treated with AuNPs to those which underwent a pulse of AuNP incubation of various times (15 min to 72 h) as well as those which had an additional depletion phase of 24 to 72 h following an incubation pulse of 72 h. The trypan blue assay is based on the integrity of the plasma membrane of live cells[3]. Employing this assay (Figure S2A) we found that the viability of cells treated under different conditions with AuNPs was always higher than 94 % for all conditions.

Secondly, the resazurin assay was employed which evaluates the metabolic function of cells based on the reduction of resazurin due to mitochondrial activity, emitting detectable, fluorescent signals[4]. The metabolic activity was determined at different time points, as shown in Figure S2B. Generally, the metabolic activity seemed to remain constant, but showed a strongly increased value after 72 h of AuNPs incubation. Such an impact was however reversible and disappeared after 24 h of AuNP withdrawal. Considering the results from the trypan blue assay (Figure S2A), this increased metabolic activity after 72 h of AuNPs exposure although interesting does not indicate cellular death, which would have caused a decrease in activity.

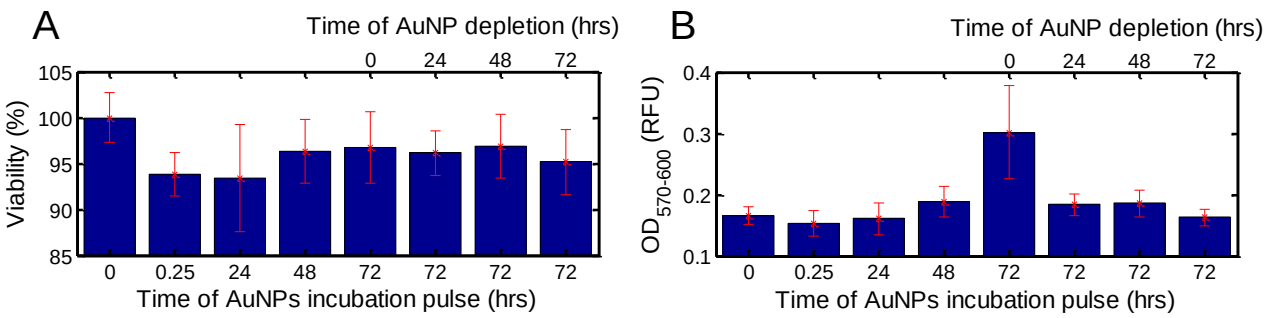

Figure S2: Viability assays on cells with AuNPs. (A) Trypan blue assay carried out for different incubation times with six repeats for each condition, showing slightly increased viability for samples treated with AuNPs but importantly all samples used for experimental purposes had a viability above 94%. (B) Resazurin assay to evaluate metabolic function of the cells showed no cell death but a mild progressive stress (increase in activity) especially at 72 h with increasing incubation times. However, such an effect was reversible and disappeared after 24 h of AuNPs depletion. Bars and whiskers indicate: (mean value ± standard deviation from six replicates).

Feature extraction methodology using PCA-LDA for R6G on Si sample. Here, we demonstrate the methodology for the extraction of unknown features from a hyperspectral dataset with respect to the generation of a pseudo-color map from a reference generated SERS/Raman datasets of known spectral features or characteristics on a simple non-biological sample. Rhodamine 6G (R6G) solution was dried on a silicon (Si) substrate to generate islands of it dispersed sporadically over the surface as shown in Figure S3A.

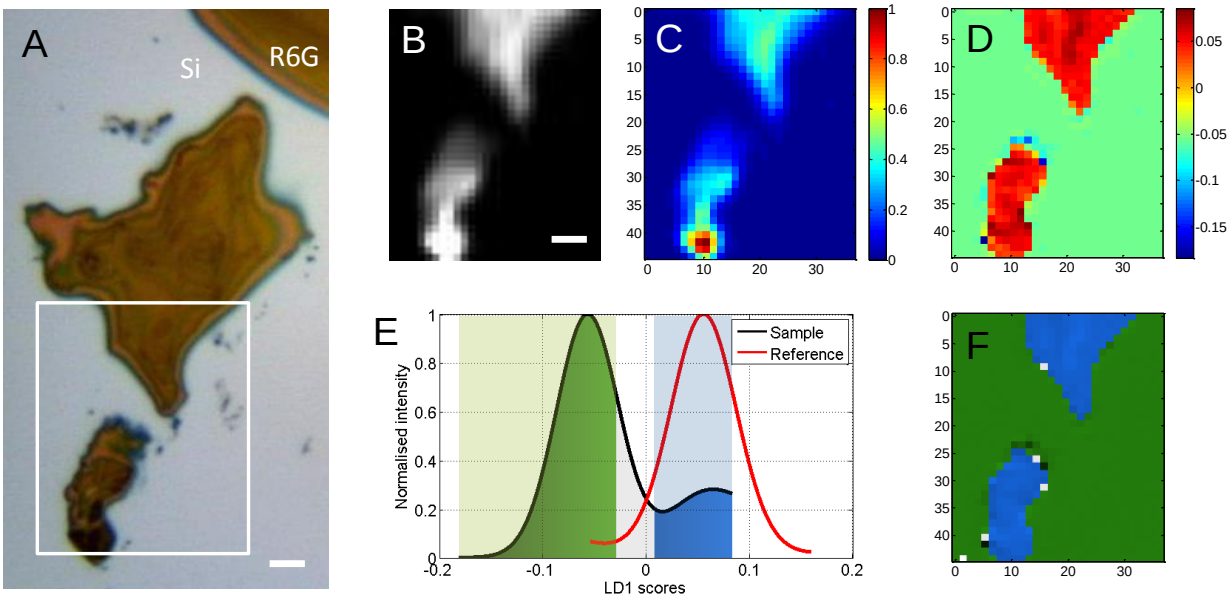

Figure S3: R6G dried on a Si surface (A) used for methodology development and validation. (B) SERS map of intensity at ~1360 cm^{-1}, which is a typical peak for R6G, but not Si. A color map of PC1 scores (C) shows not as clear differences between Si and R6G compared to the map of PCA-LDA scores (D). (E) LD1 scores distribution with assigned regions obtained by analyzing pure Si (reference) and R6G with Si (sample). LD1 scores corresponding to the reference region in (E) are colored in blue, LD1 scores which are not explained by the reference are colored in green. (F) The back-projected, color-coded LD1 scores map reveals the spatial distribution of Si (green) and R6G (blue) within the map. (A-B) Scale bar: 10 µm (C, D, F) pixel size: 600 nm x 600 nm.

First, spectra from R6G only were taken and used to form the reference state. A Raman map of the Si-R6G sample

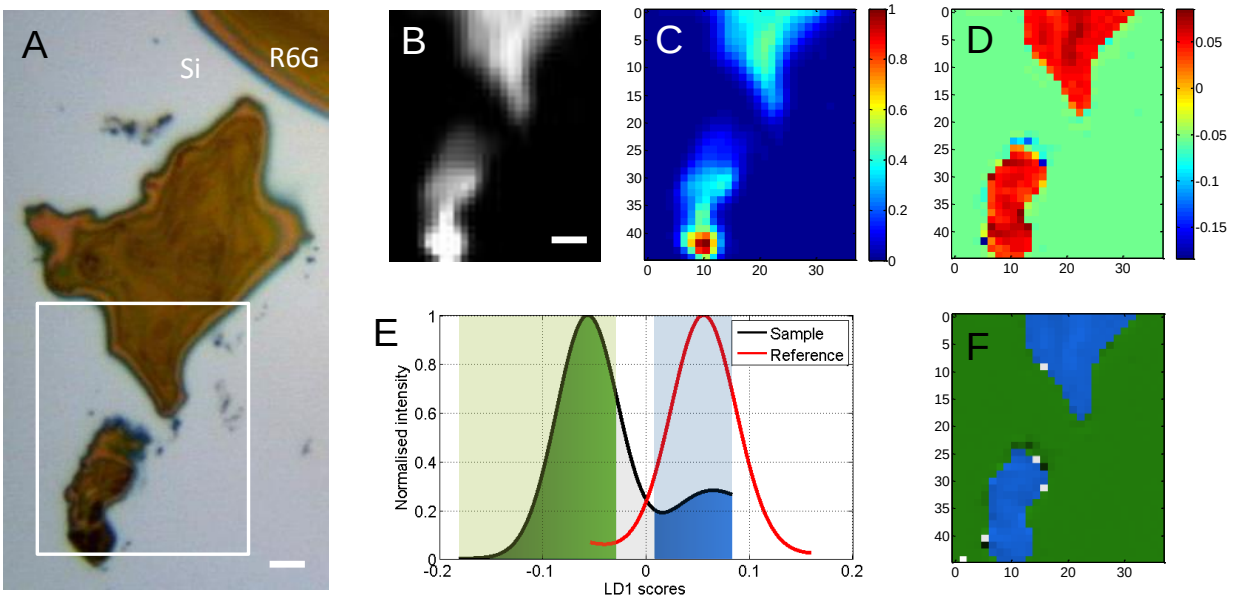

Figure S3B) was acquired from the area highlighted in

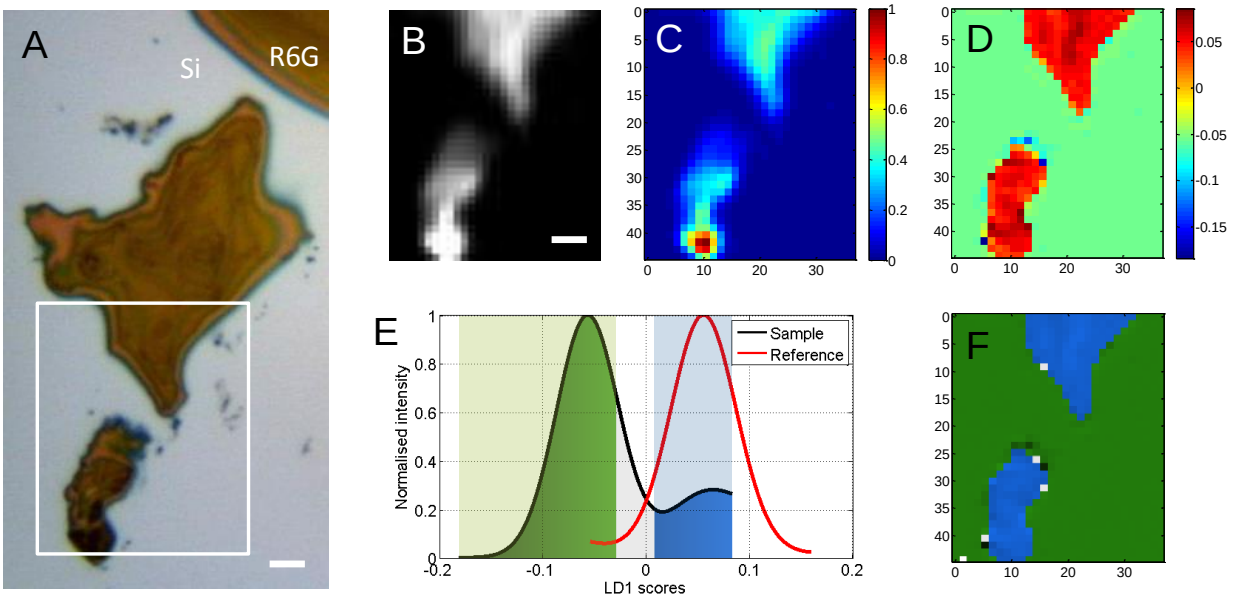

Figure S3A showing the measured intensity of the ~1360 cm^{-1} peak which is characteristic for the in-plane C-H bend of the xanthene ring stretch in R6G[5]. For further data analysis involving PCA and PCA-LDA, hyperspectral data was baseline-corrected, mean-centered and vector-normalized (only for PCA-LDA). Using PCA only as shown in

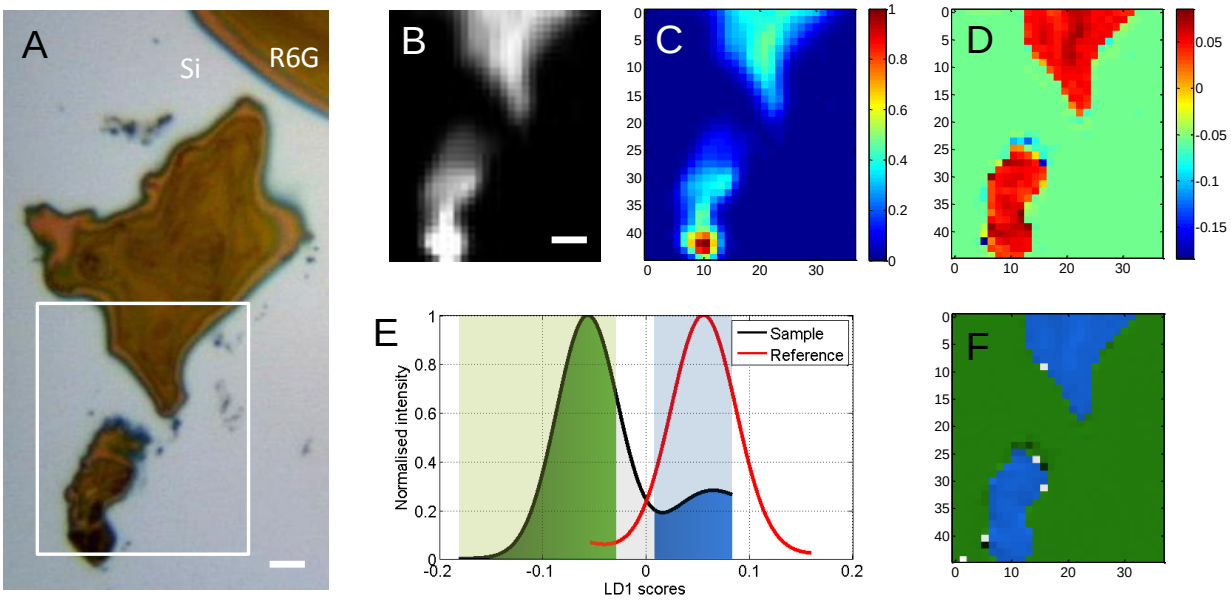

Figure S3C, it was not possible to clearly separate both components; therefore this cannot be the basis of a universal methodology applicable to further unknown samples. Due to the simplicity of the sample, PCA-LDA alone allows for the distinction of both components as shown in Figure S3C. Achieved color distinction was used as an objective for an improved and universal methodology using our reference-based PCA-LDA method. Datasets of the R6G reference and the Si-R6G sample were analyzed together using PCA-LDA. Every spectra from each group is assigned a LD1 scores value. 1D intensity curves of the resulting LD scores were generated by using the kernel density estimation (bandwidth = 1000) to smooth LD scores histograms (with a bin size of 50) as shown in

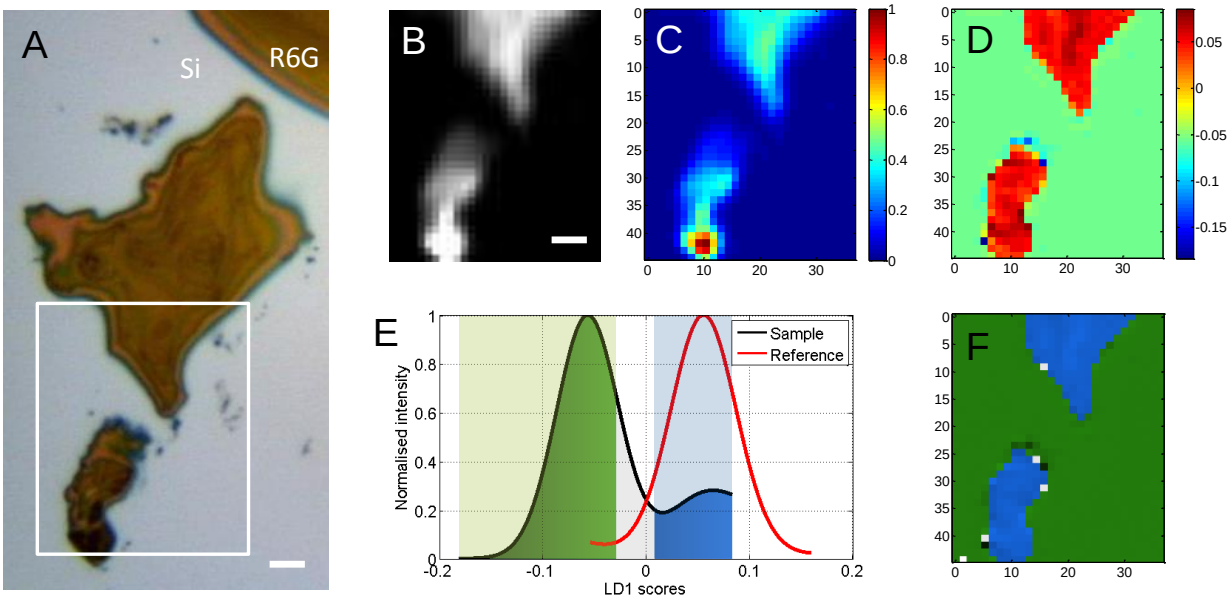

Figure S3E. Subsequently, smoothed histograms were fitted with single or multiple Gaussians depending on the goodness of fit.

Here, we used a single Gaussian and double Gaussian fit for the reference and the Si-R6G samples, respectively. Generally, overlap of these curves can be interpreted as showing common features or origin of scores underlying the spectra. Overlapping regions were used to identify R6G spectra within the sample dataset as well as non-overlapping regions to discriminate Si spectra. The general mathematical discrimination rules are as following: 1) Known features (colored in blue in

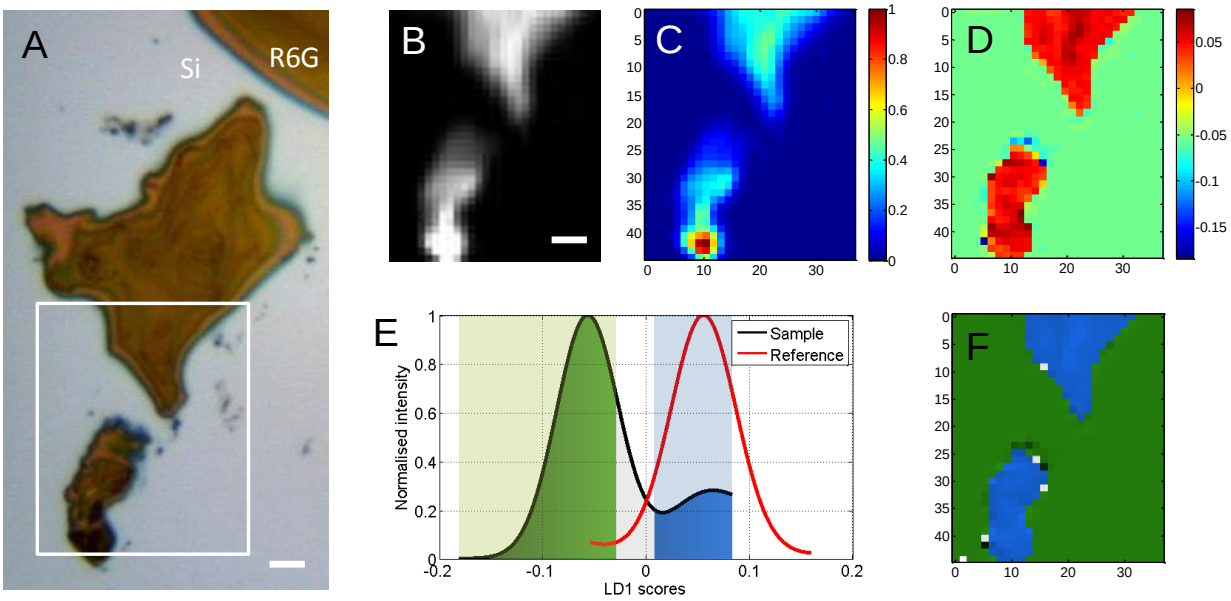

Figure S3E) are found within three standard deviations starting from the mean of the fitted curve. 2) Unknown features (here, Si in green in

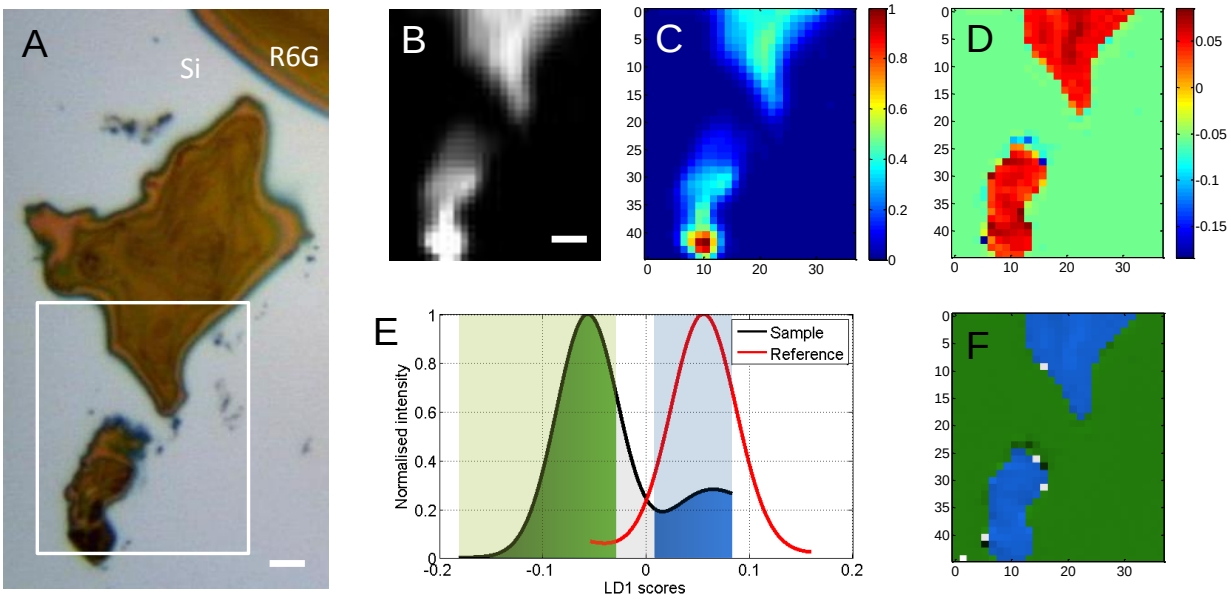

Figure S3E) are defined based on the curve fit parameters of the sample curve. They are located inside the region which is within twice the standard deviation, starting from the belonging peak center of the furthermost peak (of the sample curve) from the reference curve, but not extending into the already assigned (blue) region. 3) Regions which were not assigned according to rule 1) and 2) are a transition region. These rules were then used to assign colors to the appropriate

scores values highlighted in the scores intensity plot in

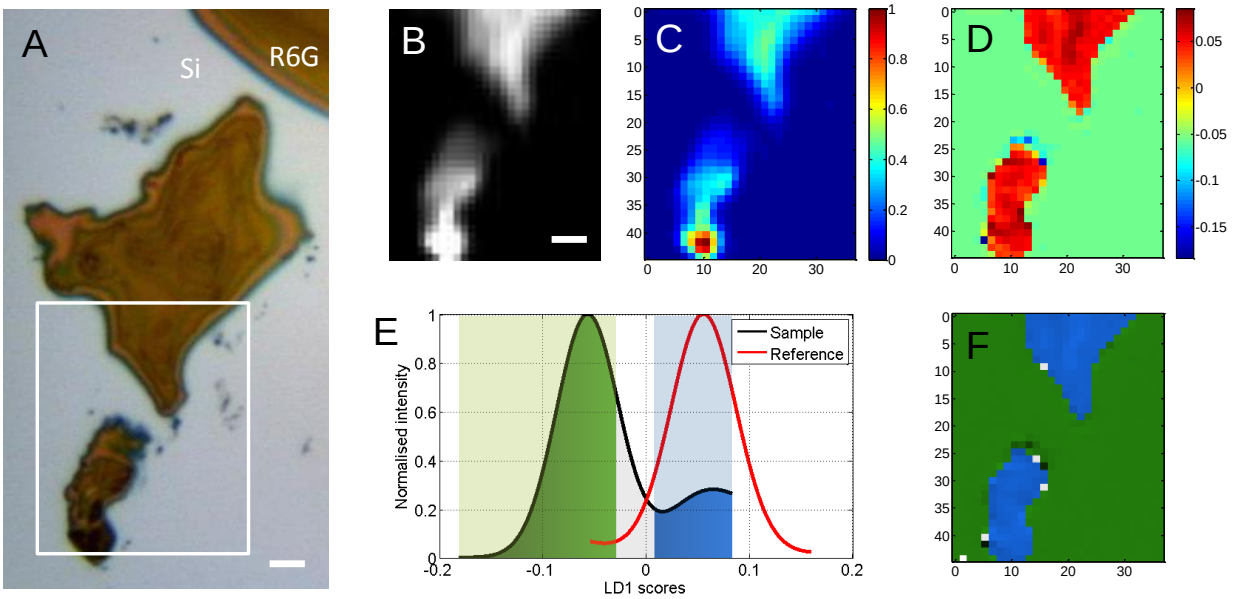

Figure S3E. Back-projection into a pseudo-color map as seen in

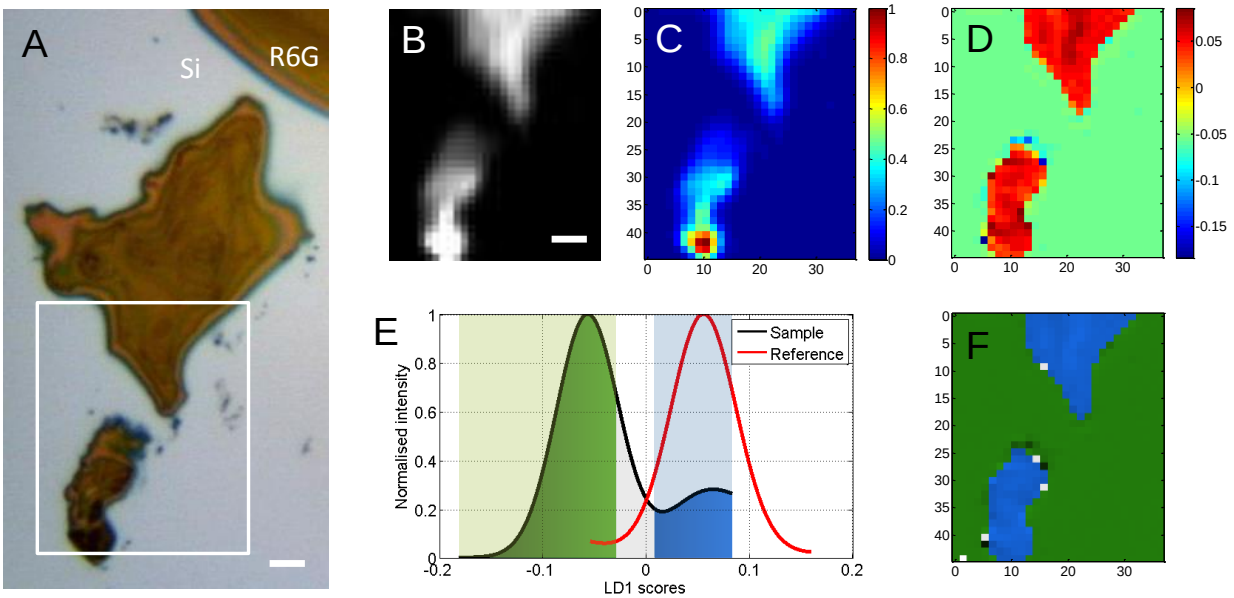

Figure S3F now shows the spatial location as well as a clear distinction of each component (Si in green, R6G in blue) in the Si-R6G sample map. The generated pseudo-color map in

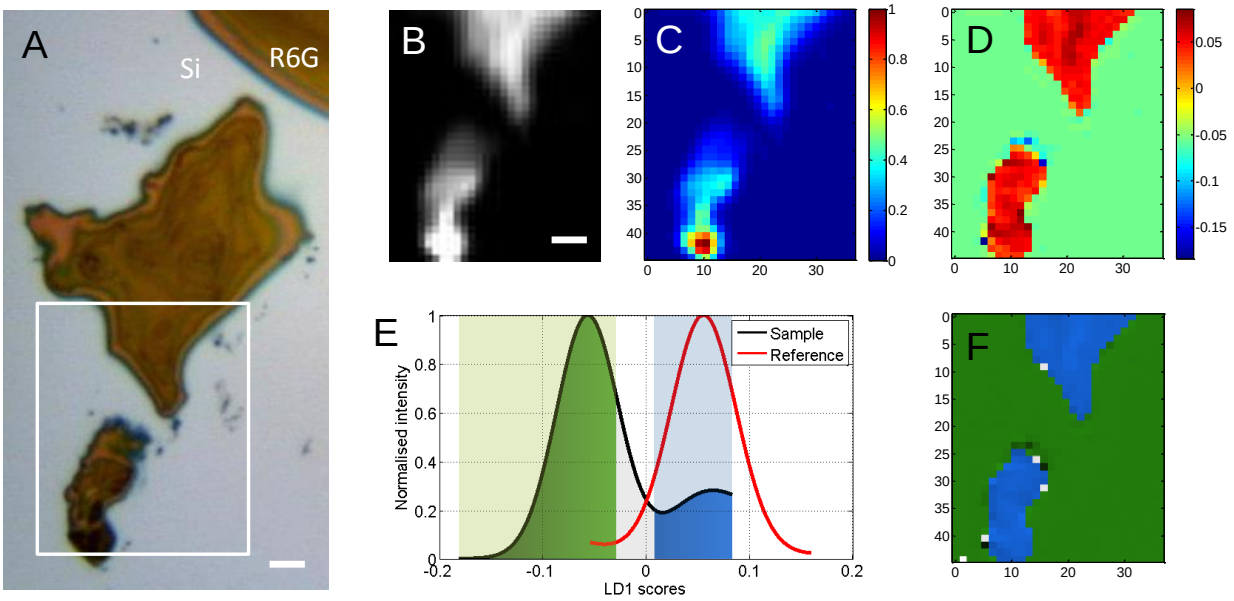

Figure S3F is in perfect agreement with the LD1 scores map in

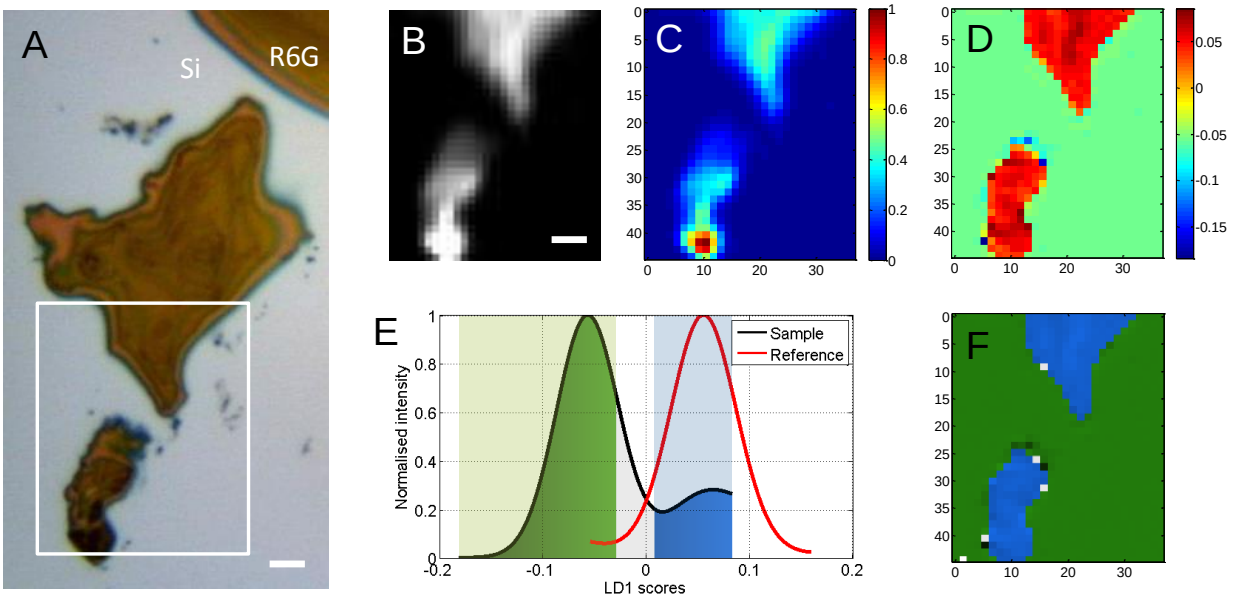

Figure S3D. Therefore, the PCA-LDA reference-based differential analysis allows for the outlining of known features within a SERS map while also including an unknown component. Furthermore, the extraction of spectra characterizing the new component can be facilitated.

Methodology adaptation to complex samples. This simple methodology was then adapted to facilitate more complicated samples as is seen with SERS datasets from inside cells. First, LD1 scores intensity histograms require the adaptation of fit parameters towards multi-peak Gaussian fitting because cell samples have a higher number of internal components or features. Primarily, this refers to the fact that both classified routes (endosomal or lysosomal pathway) still undergo different stages of maturation and fusion processes resulting in some kind of molecular and spectral diversity. These differences cause the LD1 scores intensity distribution to show multiple peaks and/or shoulders. Figure S4A shows the smoothed histograms of a sample of a cell with AuNPs in the endosomes and lysosomes (blue dash-dotted line) and the lysosomes only reference group (blue dashed line) and the double Gaussian fits (dashed black and red line, respectively) used for the example described in Figure 3-4 in the main paper. Therefore, smoothed histograms of LD1 scores of the sample cell as well as the reference were obtained as shown in Figure S4A. The intensity plot suggests a two-component Gaussian mixture distribution in both cases. To obtain a statistical characterization of the intensity plot, a double Gaussian distribution is fitted to the line plot with

$$y(x) = \sum_{i=1}^{2} h_i \cdot e^{-\frac{(x-\mu_i)^2}{2\sigma_i^2}}$$

where h_i is the mixture coefficient or peak heights. Further, μ_i is the mean and σ_i is the standard deviation of the mode i. Indices are increasing with decreasing peak heights h_i of the curve fit for positive skew of the reference curve (*i.e.* the major mode is associated with fit parameters of index 1). For negative skew of the reference curve, indices decrease with increasing peak heights. The hypothesized double Gaussian distribution was tested by determining the goodness-of-fit. The R-squared test (R^2) was calculated for the sample and reference data. In this context,

the R^2 test describes the discrepancy between the data and the expected values for the double Gaussian distribution. The R^2 is 0.993 and 0.997, respectively. This was tested for 20 further cells (after AuNP incubation pulse of 72 h) samples to verify its general validity. The mean standard deviation of R^2 is (0.993 ± 0.010) for the samples and (0.997 ± 0.002) for the reference. These R^2 values (max. 1) confirm that the LD1 scores intensity distributions can be modelled as double Gaussians for the analysis of the cell sample(s) as well as for the reference.

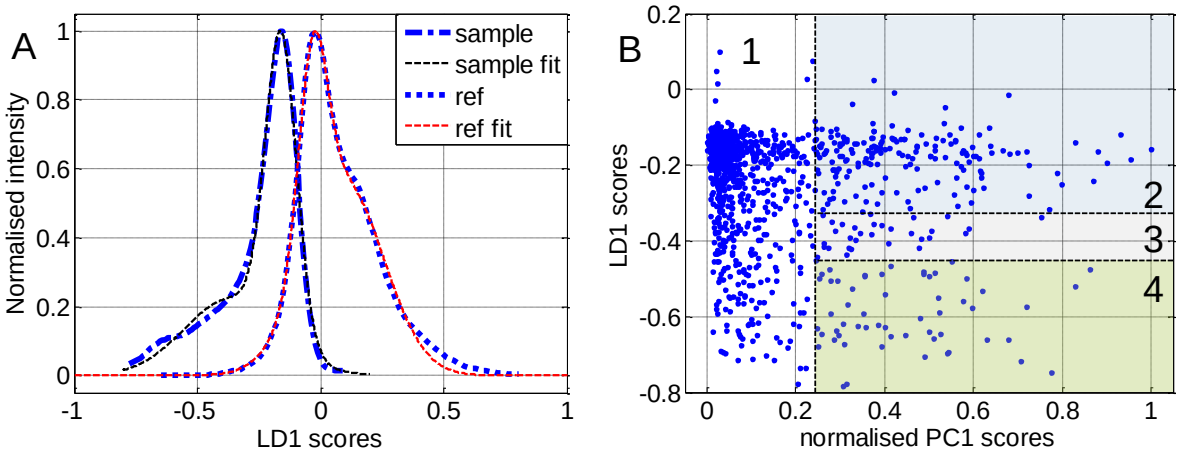

Figure S4: (A) Normalized LD1 scores intensity plots of the smoothed histograms (blue dashed and dashed-dotted lines) and appropriate double Gaussian fit. (B) PC1 *vs.* LD1 scores plot of the sample (see also Figure 4 in main paper) highlights the assigned regions 1 to 4 as sample background, lysosomes only, transition region and endosomes only, respectively.

Using the same sample cell, the PC1 scores *vs.* LD1 scores plot in Figure S4B shows clearly that there is no direct correlation between the lower 25 % of the PC1scores values (region 1 in Figure S4B) and specific LD1 values, making it necessary to use PC1 scores for sample background exclusion. Furthermore, assigned regions for lysosomes only, transition area and endosomes only are found in region 2 - 4. Data has been taken from the same sample as used for Figure 3-4 in the main paper.

Validation of our methodology. In order to show further validation of the method used in this study, a negative control, meaning that the sample only comprises of one component/class, is shown in Figure S5. For this purpose, we used a cell sample which has undergone 48 h of AuNP depletion after 72 h of particle incubation pulse which was not included in the reference dataset used for the analysis in the main paper, but produced under the same experimental conditions. Here, the hypothesis being tested is to find only lysosome specific spectra in the dataset.

A bright field image of the sample cell and the SERS map of the protein band at around 1400 cm^{-1} are shown in Figure S5A-B, respectively. Figure S5C shows the PC1 scores map of the same sample with the sample background excluded (colored in white) revealing the location of particle-based SERS signals from inside the cell. LD1 scores mapping the distribution and intensity curves are shown in Figure S5D-E. The LD1 scores intensity curve completely overlaps with the reference. Class assignments according to the methodology introduced above reveal only one region (blue) as seen in Figure S5F. Additionally, the back-projection into a pseudo-color map in Figure S5F now outlines the localization of AuNPs inside the lysosomes. This result is in accordance with our hypothesis.

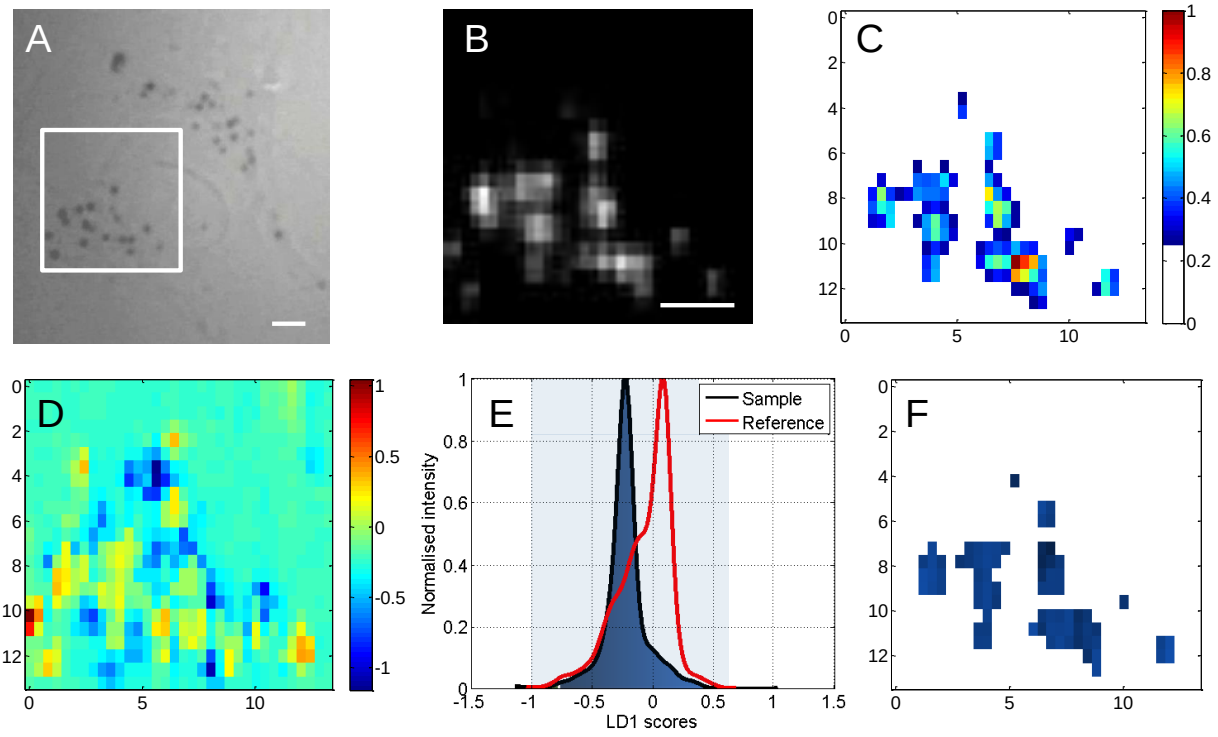

Figure S5: Bright field image (A) of a cell after a 72 h AuNPs incubation pulse and 48 h of AuNPs depletion. The white box outlines the area imaged using SERS mapping. (B) SERS map showing the spatial distribution of the protein band around 1400 cm^{-1}. (C) PC1 scores distribution with a sample background colored in white (the lower 25 % of all PC1 scores). LD1 scores map distribution (D) and LD1 intensity curves of the cell sample (black line) and the reference (red line) (E) showing complete overlap of reference and sample as indicated by the blue shade and fill of the sample curve. (F) Back-projection of assigned LD1 scores results in a pseudo-color map outlining the spatial distribution of particles and their localization inside the sample area. (A-B) scale bar: 10 µm. (C-D, F) pixel size: 600 nm x 600 nm.

Molecular characterization of the endosomal and lysosomal pathways. The validity of the developed analysis method is exemplarily shown for the extraction of spectra and the subsequent characterization of molecular features in endosomal and lysosomal vesicles. Extracted data sets

of SERS spectra originating from either endosomes (n=1817) or lysosomes (n=3503) were mean-centred and PCA was applied. To assess the variation within each group, PC1 loadings of subsets of the group data were compared, as shown for endosomal spectra in Figure S6A. Subsets consist of 1000 randomly selected spectra. The standard deviation of six repeats, as shown in Figure S6B, is indicated in the main paper as red shaded area to the group PC1 loadings (Figure 5A).

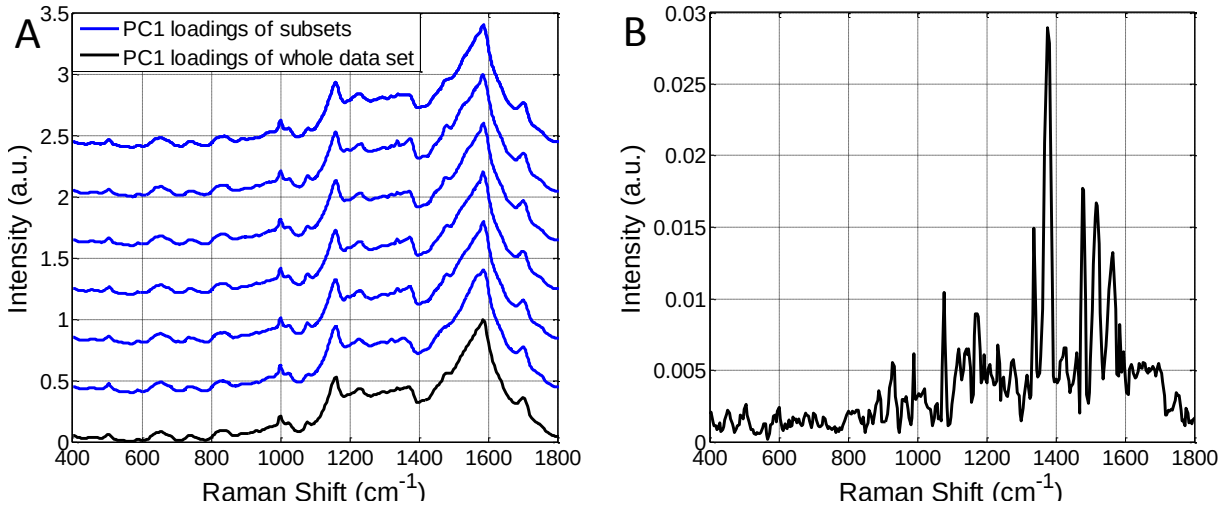

Figure S6: For SERS from endosomes, PC1 loadings of the whole data set (blue) and six subsets (black line, A) were generated. Based on the PC1 loadings of the subsets, the standard deviation (B) was calculated.

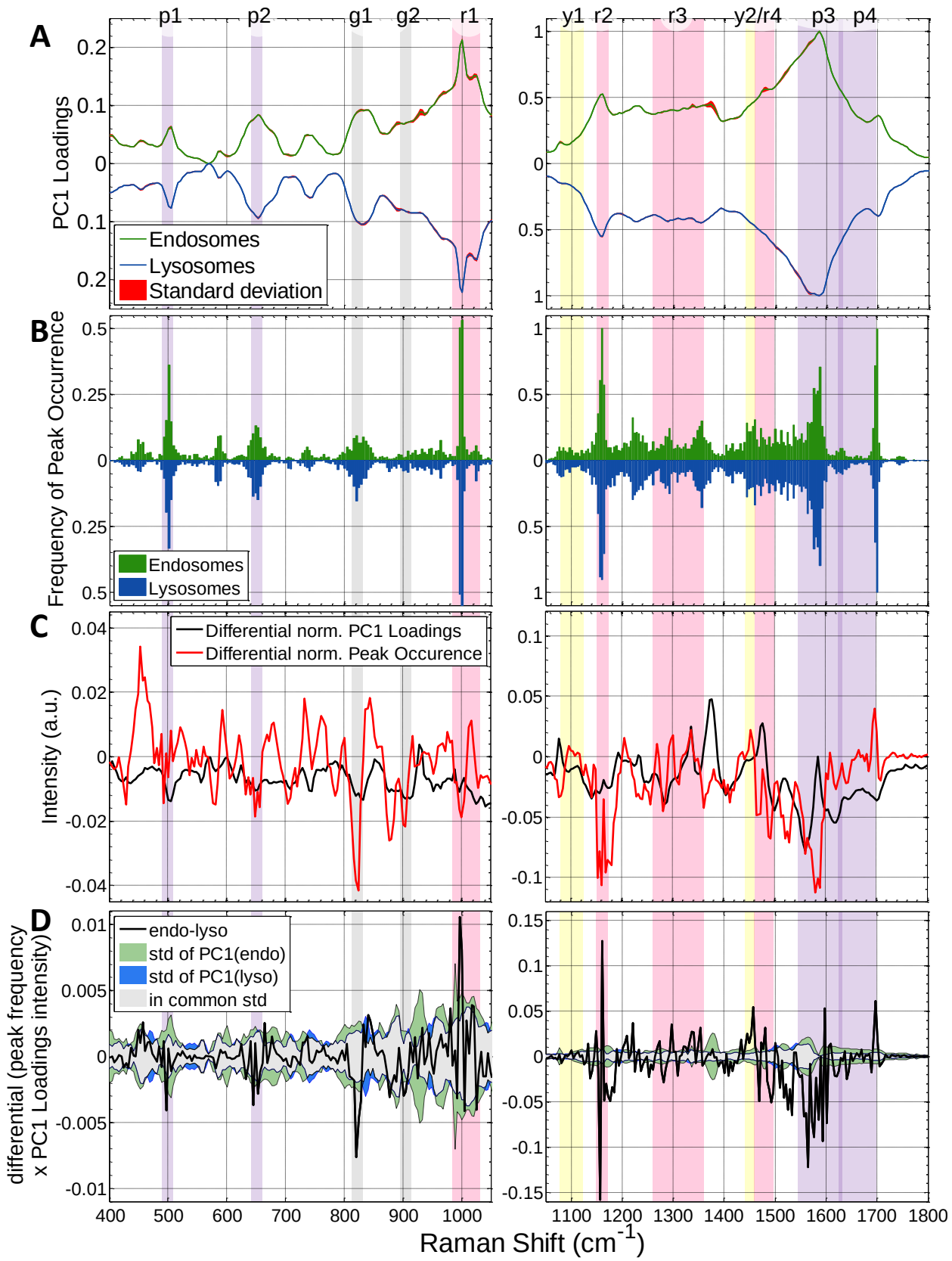
A
B
C
D
p1
p2
g1
g2
r1
y1
r2
r3
y2/r4
p3
p4
PC1 Loadings
Endosomes
Lysosomes
Standard deviation
Frequency of Peak Occurrence
Endosomes
Lysosomes
Differential norm. PC1 Loadings
Differential norm. Peak Occurence
Intensity (a.u.)
endo-lyso
std of PC1(endo)
std of PC1(lyso)
in common std
differential (peak frequency x PC1 Loadings intensity)
Raman Shift (cm-1)

Figure S7: For endosomes (green) and lysosomes (blue), the normalized PC1 loadings and standard deviation (A) as well as the normalized frequency of peak occurrence (B) have been used to calculate the differential (normalized) PC1 loadings and (normalized) peak frequency (C). To account for major differences between both groups and combining information about the peak probability (B) with information about peak intensities and ratios (PC1 loadings, A), the frequency of peak occurrence was weighted by the PC1 loadings before calculating the difference between the two groups (D). Selected major differences between endosomes and lysosomes, based on (A-D), are highlighted in purple, grey, red and yellow (for details see main paper).

Spectral differences of the endolysosomal pathway and their assignments. In order to capture the spectral differences between both groups, SERS originating from endosomes and lysosomes, the analysis is based on the PC1 loadings (Figure S7A) and the frequency of peak occurrence (Figure S7B). The differential PC1 loadings and peak frequency (Figure S7C) indicates differences between both groups. To include information from both methods of analysis, PCA and peak frequency, Figure S7D shows the frequency of peak occurrence weighted by the PC1 loadings prior to calculating the difference between endosomes and lysosomes. The regions highlighted in purple, grey, yellow and red (Figure S7D) were chosen under consideration of Figure S7C-D and exceeding of the standard deviation for detailed analysis/interpretation in the main paper.

In Table 1, major spectral differences and peak shifts as well as their molecular assignments are presented.

Table 1: Assignments for differential frequencies of endosomal and lysosomal spectra. Abbr.; v: vibration, d: deformation, w: wagging, t: torsion, as: asymmetrical, s: symmetrical.

Prominent peak (in cm^{-1})		assignments	Specific meaning/explanation in the context of endosome-lysosome pathway
Lysosomal pathway	Endosomal pathway		
	~450	- skeletal *v*(C-C) of peptides and lipids[6]	- connected with 1160 cm^{-1} peak which remains constant, but is pH sensitive as it undergoes a small shift[7]
	~500	- *v*(S-S)[8, 9]	- break- down of polypeptides
~580	~590	- *w*(COOH)[6]	
	582-600	- skeletal in-plane *d*(C-C-C-C)[10]	- decrease as broken down into smaller fragments[10]
630, 705-709		- *v*(C-S)[6]	- breakdown of polypeptides
	729-740	- *d*(COOH)[6]	
808-830		- *v*(PO_2^-)[11, 12]	-DNA/RNA
	833-845	- *v*(C-C), *t*(CH_2), *r*(NH_3^+)[6]	
865	877	- *v*(C-C)[10]	- shift due to skeletal changes during peptide digestion[10]
880-910		- Ribose phosphate[11, 12]	- backbone of DNA/RNA
	~980	- *v*(PO_2^-)[7]	- pH induced[7]
	997-1003	- v_s(C-C), phe[6, 13] -v(C-N)[14]	- *v*(C-C) remains constant[10] or decreases slightly due to digestion of polypeptides
1025-1030	1010-1020	- *v*(PO_2^-)[7]	- Phosphate peak is pH sensitive[10]
1077-1082	1088-1100	- v_s(PO_2^-), *v*(C-C)[6, 15, 16]	- breakdown of lipid bilayers
~1120	1125-1130	- skeletal *v*(C-C)[16]	- skeletal stretching mode region is sensitive intrachain disorder[16]
1157	1161	- *v*(C-C)[10] overlaid with *v*(C-N)[17], *d*(NH_3^+)[18]	- change in backbone frequency due to change in environment (eg pH)[18, 19]
	~1220	- v_{as}(PO_2^-)[13], *d*(C-C_a-N)[6]	
1237		- β-sheet[20]	- Breakdown of proteins
1253		- Random coil[20]	- Breakdown of proteins
1275-1285	1285-1300	- in-plane *v*(C-H), *v*(C-N)[17, 21]	- pH induced shift
1370	1324, 1349-	- *v*(C=N) and *w*(CH_2)[17]	- pH induced shift

	1357		
	1340-1355	- ν(C-C) skeletal mode[17] overlaid with in-plane d(O-H)[18]	- breakdown of proteins and lipids[17] - pH sensitive[18]
	1440-1460	- $d(CH_2)$, $d(CH_3)$, backbone of phospholipids[13]	- breakdown of lipids
1485-1491	1472-1482	- in-plane b(C=N)[17]	- Imidazole skeletal mode in histidine shifts due to more acidic pH[17]
	1515-1535	- $d_s(NH_3^+)$[6]	
1535-1555		- $\nu(COO^-)$[22, 23]	
1585	1589	- $\nu_{as}(COOH)$[6] to $\nu(COO^-)$[22]	- pH
1617-1625		- ν(C=C), try[13]	
	1629-1637	- Amide I, a-helix structure[20]	- Breakdown of proteins results in breakdown of α-helix structure
1695-1703	1640-1645	- $d_{as}(NH_3^+)$, amino acids[6] - Amide I is more accessible in smaller peptides than in proteins[24]	- pH induced N-H peptide group motion[23]
1673		- Random coil[20]	
1721-1725	1741-1753	- ν(C=O) in phospholipids[10, 13, 16, 18, 23, 25] - shifted to 1745 due to pH?[25]	- breakdown of lipid bilayers/membrane fractions results in shift towards lower wavenumbers[10, 16, 18, 26] - corresponds to 1440-1460cm^{-1} region

References

1. Krysko, D. V.; Berghe, T. V.; Parthoens, E.; D'Herde, K.; Vandenabeele, P. Chapter 16 Methods for Distinguishing Apoptotic from Necrotic Cells and Measuring Their Clearance. In *Method Enzymol*, Roya Khosravi-Far, Z. Z. R. A. L.; Mauro, P., Eds. Academic Press: 2008; Vol. Volume 442, pp 307-341.
2. Elmore, S. Apoptosis: A Review of Programmed Cell Death. *Toxicol Pathol* 2007, 35, 495-516.
3. Strober, W. Trypan Blue Exclusion Test of Cell Viability. *Curr Protoc Immunol* 2001, Appendix 3, Appendix 3B.
4. Nociari, M. M.; Shalev, A.; Benias, P.; Russo, C. A Novel One-Step, Highly Sensitive Fluorometric Assay to Evaluate Cell-Mediated Cytotoxicity. *J Immunol Methods* 1998, 213, 157-67.
5. Jensen, L.; Schatz, G. C. Resonance Raman Scattering of Rhodamine 6g as Calculated Using Time-Dependent Density Functional Theory. *J Phys Chem A* 2006, 110, 5973-5977.
6. Podstawka, E.; Ozaki, Y.; Proniewicz, L. M. Part Iii: Surface-Enhanced Raman Scattering of Amino Acids and Their Homodipeptide Monolayers Deposited onto Colloidal Gold Surface. *Appl Spectrosc* 2005, 59, 1516-1526.
7. Xie, Y.; Jiang, Y.; Ben-Amotz, D. Detection of Amino Acid and Peptide Phosphate Protonation Using Raman Spectroscopy. *Anal Biochem* 2005, 343, 223-230.
8. Lin, V. J. C.; Koenig, J. L. Raman Studies of Bovine Serum Albumin. *Biopolymers* 1976, 15, 203-218.
9. Tu, A. T. Use of Raman Spectroscopy in Biological Compounds. *J Chin Chem Soc* 2003, 50, 1-10.
10. Ravikumar, B.; Rajaram, R. K.; Ramakrishnan, V. Raman and Ir Spectral Studies of L-Phenylalanine L-Phenylalaninium Dihydrogenphosphate and Dl-Phenylalaninium Dihydrogenphosphate. *J Raman Spectrosc* 2006, 37, 597-605.
11. Verrier, S.; Notingher, I.; Polak, J. M.; Hench, L. L. *In Situ* Monitoring of Cell Death Using Raman Microspectroscopy. *Biopolymers* 2004, 74, 157-62.
12. Boyd, A.; McManus, L.; Burke, G.; Meenan, B. Raman Spectroscopy of Primary Bovine Aortic Endothelial Cells: A Comparison of Single Cell and Cell Cluster Analysis. *J Mater Sci-Mater M* 2011, 22, 1923-1930.
13. Huang, Z.; McWilliams, A.; Lui, H.; McLean, D. I.; Lam, S.; Zeng, H. Near-Infrared Raman Spectroscopy for Optical Diagnosis of Lung Cancer. *Int J Cancer* 2003, 107, 1047-1052.
14. Dou, X.; Jung, Y. M.; Yamamoto, H.; Doi, S.; Ozaki, Y. Near-Infrared Excited Surface-Enhanced Raman Scattering of Biological Molecules on Gold Colloid I: Effects of Ph of the Solutions of Amino Acids and of Their Polymerization. *Applied spectroscopy* 1999, 53, 133-138.
15. Socrates, G.; Socrates, G. I. c. g. f. *Infrared and Raman Characteristic Group Frequencies : Tables and Charts*. 3rd ed.; Wiley: Chichester, 2001; p xv, 347 p.
16. Carrier, D.; Pézolet, M. Raman Spectroscopic Study of the Interaction of Poly-L-Lysine with Dipalmitoylphosphatidylglycerol Bilayers. *Biophys J* 1984, 46, 497-506.
17. Mesu, J. G.; Visser, T.; Soulimani, F.; Weckhuysen, B. M. Infrared and Raman Spectroscopic Study of Ph-Induced Structural Changes of L-Histidine in Aqueous Environment. *Vib Spectrosc* 2005, 39, 114-125.

18. Tschirner, N.; Schenderlein, M.; Brose, K.; Schlodder, E.; Mroginski, M. A.; Thomsen, C.; Hildebrandt, P. Resonance Raman Spectra of [Small Beta]-Carotene in Solution and in Photosystems Revisited: An Experimental and Theoretical Study. *Phy Chem Chem Phys* 2009, 11, 11471-11478.
19. Hahn, D. W.; Wolfarth, D. L.; Parks, N. L. Analysis of Polyethylene Wear Debris Using Micro-Raman Spectroscopy: A Report on the Presence of Beta-Carotene. *J Biomed Mater Res* 1997, 35, 31-7.
20. Maiti, N. C.; Apetri, M. M.; Zagorski, M. G.; Carey, P. R.; Anderson, V. E. Raman Spectroscopic Characterization of Secondary Structure in Natively Unfolded Proteins: A-Synuclein. *J Am Chem Soc* 2004, 126, 2399-2408.
21. Stewart, S.; Fredericks, P. M. Surface-Enhanced Raman Spectroscopy of Peptides and Proteins Adsorbed on an Electrochemically Prepared Silver Surface. *Spectrochim Acta A* 1999, 55, 1615-1640.
22. Castro, J. L.; Ramírez, M. R. L.; Arenas, J. F.; Otero, J. C. Vibrational Spectra of 3-Phenylpropionic Acid and L-Phenylalanine. *Anglais* 2005, 744–747, 887-891.
23. Garfinkel, D.; Edsall, J. T. Raman Spectra of Amino Acids and Related Compounds. X. The Raman Spectra of Certain Peptides and of Lysozyme1-3. *Journal of the American Chemical Society* 1958, 80, 3818-3823.
24. Kurouski, D.; Postiglione, T.; Deckert-Gaudig, T.; Deckert, V.; Lednev, I. K. Amide I Vibrational Mode Suppression in Surface (Sers) and Tip (Ters) Enhanced Raman Spectra of Protein Specimens. *Analyst* 2013, 138, 1665-1673.
25. Edsall, J. T.; Otvos, J. W.; Rich, A. Raman Spectra of Amino Acids and Related Compounds. Vii. Glycylglycine, Cysteine, Cystine and Other Amino Acids. *J Am Chem Soc* 1950, 72, 474-477.
26. Mushayakarara, E.; Albon, N.; Levin, I. W. Effect of Water on the Molecular Structure of a Phosphatidylcholine Hydrate. Raman Spectroscopic Analysis of the Phosphate, Carbonyl and Carbon-Hydrogen Stretching Mode Regions of 1,2-Dipalmitoylphosphatidylcholine Dihydrate. *Biochim Biophys Acta* 1982, 686, 153-9.